

# Electrical Prism: A High Quality Factor Filter for Millimeter-Wave and Terahertz Frequencies

Omeed Momeni, *Student Member, IEEE*, and Ehsan Afshari, *Member, IEEE*

**Abstract**—A 2-D electrical filter is introduced that is compatible with today's conventional integrated circuit processes. The rich 2-D propagation properties of the medium are used to introduce a novel high quality factor filter called an *electrical prism*. The proposed filter shows a quality factor much larger than the quality factor of the individual components at high millimeter-wave and terahertz frequencies. This structure also provides a negative effective index in a low-pass *LC* lattice. Based on this idea, we show filters with quality factors of 130 at 230 GHz and 420 at 460 GHz consisting of elements with the quality factor of 10 and 20, respectively. The effect of component loss on the filter quality factor is discussed in this paper. The negative effective index and the filter behavior of the lattice is verified by measuring a prototype on a CMOS process at 32–40 GHz. There is good agreement among the theory, simulation, and experimental results.

**Index Terms**—CMOS, dispersion, electrical prism, high quality factor filter, negative effective index, spatial filtering, terahertz, 2-D electrical lattice.

## I. INTRODUCTION

THE TERAHERTZ frequency range is usually defined to be from 100 GHz to 10 THz. Bio-spectroscopy and molecular spectroscopy were the first and the main applications for the terahertz region [1]. Recently, this range has also been used for imaging, compact range radars, and remote sensing [2]–[5]. Traditionally, the solid-state version of all these systems, along with the terahertz sources, have been built using III–V-based HBT/HEMT technologies like GaAs [2]. As the CMOS technology scales down, the  $f_{\max}$  of the transistors are reaching the lower part of the terahertz range: the 65-nm CMOS technology already has an  $f_{\max}$  of around 200 GHz [6]. The CMOS scaling along with the III–V technology drawbacks such as cost and efficiency paved the way for the recent terahertz work in silicon processes [7], [8].

The 2-D electrical lattices are 2-D discrete lattices in which the building block is constructed using passive elements. Fig. 1 is an example of a 2-D lattice. Each line represents an inductor, and each dot represents a capacitor to ground. This specific lattice is a low-pass lattice, but other lattices with different frequency responses can be constructed. The 2-D electrical lattices

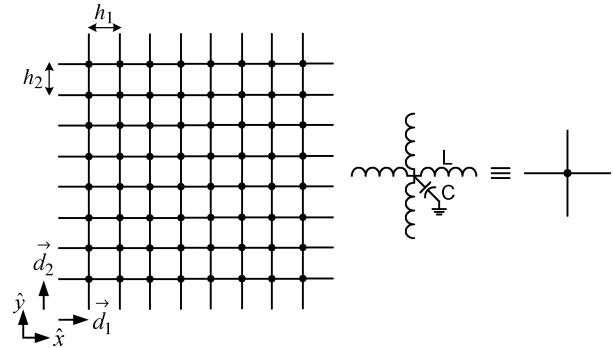


Fig. 1. Rectangular *LC* lattice.

on silicon have a potential in terahertz signal generation and processing due to their distributed nature and their scalability for higher frequencies. Several studies have shown that this class of circuits is promising for high frequencies. In terms of signal generation, [9] illustrates the highest output power for a power amplifier for the wide band of 60–100 GHz using a 2-D electrical lattice. It is also shown in [10] that by using a well-sized nonlinear 2-D lattice, one is able to generate an output signal frequency five to six times greater than the input signal frequency. Due to the distributed nature of this lattice, the power of the input signals will add together to generate the output signal that has more power than each input. In terms of signal processing, [11] shows that using low-pass 2-D lattices it is possible to make an ultra-fast Fourier transformer for terahertz frequencies. Furthermore, [12] and [13] demonstrate compact electrical lens in high-pass and anisotropic 2-D electrical lattices, and [14] illustrates a 2-D frequency-scanned leaky-wave antenna using the same kind of 2-D lattices. Electrical lattices of this class are known as metamaterials. Interesting phenomena such as the negative refractive index is observed in metamaterials at wavelengths much larger than its unit cell dimensions [15], [16].

In all of the terahertz systems, high quality factor filters are the essential part of the operation. Furthermore, the solid-state terahertz sources use nonlinear elements for up/down conversion and multiplication to generate power. To suppress harmonics generated and to get a clean spectrum, a high quality factor filters are required. In terahertz spectroscopy, in order to find the output spectrum, a high quality factor filter bank is used. Typically, this has been done off-chip by mixing down the signal and using the filter bank at low frequencies. In order to eliminate the mixer and make a silicon-based spectrometer, a high quality factor filter at terahertz frequencies is desirable. It can be shown that the quality factor of the conventional passive filters are limited to the quality factor of the individual

Manuscript received March 18, 2009; revised June 01, 2009. First published October 06, 2009; current version published November 11, 2009. This work was supported in part by the National Science Foundation under NSF Grant DMS-0713732 and by the Defense Advanced Research Projects Agency (DARPA) under a 2007 DARPA Young Faculty Award.

The authors are with the Department of Electrical and Computer Engineering, Cornell University, Ithaca, NY 14853 USA (e-mail: om53@cornell.edu; ehsan@ece.cornell.edu).

Color versions of one or more of the figures in this paper are available online at <http://ieeexplore.ieee.org>.

Digital Object Identifier 10.1109/TMTT.2009.2032343

components [17], which is low at high frequencies due to ohmic and substrate loss in silicon processes [18].

In optics, high quality factor filters and demultiplexers have been realized using photonic crystals [19], [20]. By engineering the crystal's frequency bandgap, different frequencies will propagate in different directions in the crystal. This spatial filter is called a superprism. The light propagation in this kind of photonic crystal is very similar to that in diffraction grating [21]. In other words, the dispersion that causes the superprism effect originates from scattering (e.g., diffraction grating). In this paper, we introduce a spatial filtering method (electrical prism) using a low-pass 2-D electrical lattice. The operation of this filter relies on the dispersion in the 2-D electrical lattices. Unlike superprism, dispersion in the homogeneous 2-D electrical lattice originates from the discreteness of the lattice rather than the scattering [22]. Due to this dispersion, the direction of the energy flow is a function of signal frequency at frequencies close to the cutoff frequency. The main specifications of the proposed filter are as follows.

- The negative effective index is observed in this electrical prism.
- Unlike metamaterials, these interesting features are happening close to the cutoff frequency, which helps to channel the signal from input to output.
- The quality factor of the filter is much larger than the quality factor of each individual component in the lattice, solving one of the major challenges of the above-mentioned high-frequency filter design.
- The operating frequency of this filter can be as high as the cutoff frequency of a 2-D electrical lattice, which can reach 1.4 THz in a conventional CMOS process.

The remainder of this paper is organized as follows. In Section II, the general theory of plane-wave propagation in a low-pass 2-D lattice will be discussed. The direction of the energy will be derived for rectangular and triangular lattices. In Section III, we will show how to build an electrical prism using 2-D lattices; filter quality factor discussion, theory, and simulation plots will be provided for a lossless structure. The effect of component loss on the quality factor of the filter will be discussed in Section IV. In Section V, the design, simulation, and the measurement result of the electrical prism prototype will be presented. We will then summarize the paper in Section VI.

## II. PLANE-WAVE PROPAGATION IN 2-D LATTICES

### A. Rectangular Lattice

Fig. 1 shows a top view of a 2-D rectangular lattice. The lines represent inductors with value  $L$ , and the dots are the nodes that are connected to ground with capacitors with value  $C$ . The dot distances are  $h_1$  and  $h_2$  in the  $\hat{x}$ - and  $\hat{y}$ -directions, respectively. Coordinate vectors for the nodes  $\vec{d}_1$  and  $\vec{d}_2$  and the position vector  $\vec{r}$  are defined as follows:

$$\vec{d}_1 = h_1 \hat{x} \quad (1a)$$

$$\vec{d}_2 = h_2 \hat{y} \quad (1b)$$

$$\vec{r} = l_1 \vec{d}_1 + l_2 \vec{d}_2. \quad (1c)$$

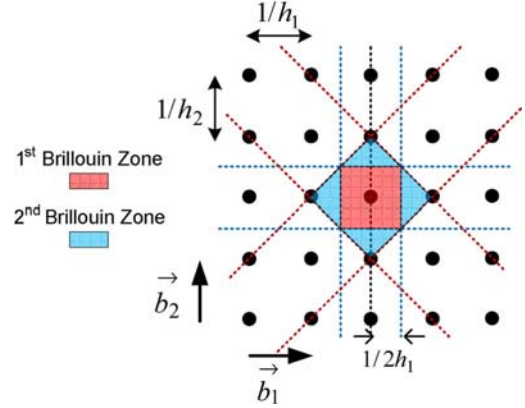


Fig. 2. Brillouin zones in reciprocal lattice for the rectangular lattice.

For the above lattice,  $l_1$  and  $l_2$  are integer numbers. For a plane wave, the voltage at each node is of the form

$$V = A \exp [i (2\pi(\vec{a} \cdot \vec{r}) - \omega t)] \quad (2)$$

in which  $\vec{a}$  is the wave vector and  $\omega$  is the angular frequency of the signal. The wave vector directly relates to wavelength  $\lambda$ , and in 2-D, it can be defined as

$$\vec{a} = a_1 \hat{x} + a_2 \hat{y} \quad (3a)$$

$$a_1^2 + a_2^2 = 1/\lambda^2. \quad (3b)$$

After substituting (1) and (3) in (2), we arrive at the equation

$$V = A \exp [i(k_1 l_1 + k_2 l_2 - \omega t)] \quad (4)$$

where  $k_1$  and  $k_2$  are the phase shifts per section in the  $\hat{x}$ - and  $\hat{y}$ -directions, respectively. The values of  $k_1$  and  $k_2$  can be given by

$$k_1 = 2\pi(\vec{a} \cdot \vec{d}_1) = 2\pi a_1 h_1 \quad (5a)$$

$$k_2 = 2\pi(\vec{a} \cdot \vec{d}_2) = 2\pi a_2 h_2. \quad (5b)$$

Using the above information, we can find the reciprocal lattice for a rectangular lattice. The reciprocal lattice is an imaginary lattice in the wave-vector space [23]. All of the points in the first Brillouin zone in the reciprocal lattice represent unique  $\vec{a}$  vectors. For any point in the second Brillouin zone, there is a corresponding point in the first Brillouin zone that represents the same plane wave. In order to analyze the lattice, it is beneficial to find the reciprocal lattice introduced in [24]. It can be easily shown that the coordinate vectors for the reciprocal lattice are

$$\vec{b}_1 = 1/h_1 \hat{x} \quad (6a)$$

$$\vec{b}_2 = 1/h_2 \hat{y}. \quad (6b)$$

Fig. 2 shows the reciprocal lattice along with the first two Brillouin zones for the rectangular lattice. It is apparent from Fig. 2 that, in the first Brillouin zone,  $a_1$  and  $a_2$  have the maximum values of  $1/2h_1$  and  $1/2h_2$ , respectively. We can find the maximum values for  $k_1$  and  $k_2$  by

$$\text{Max}\{k_1\} = 2\pi \text{Max}\{a_1\} h_1 = \pi \quad (7a)$$

$$\text{Max}\{k_2\} = 2\pi \text{Max}\{a_2\} h_2 = \pi. \quad (7b)$$

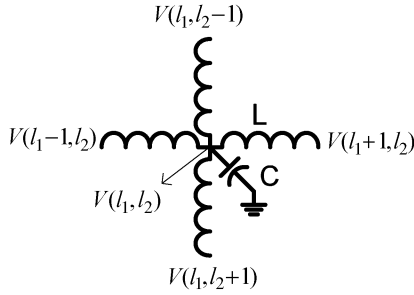


Fig. 3. Rectangular lattice cell.

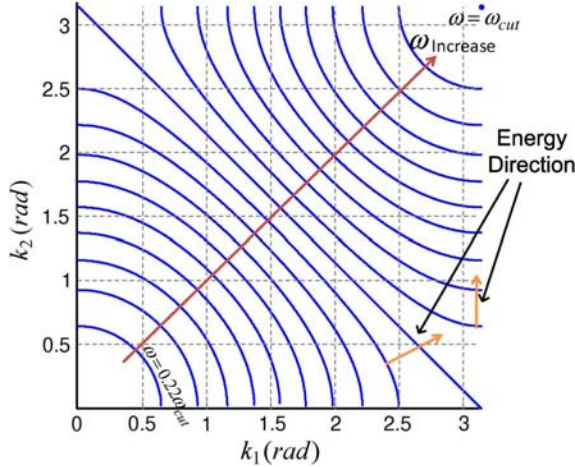


Fig. 4. Equi-frequency diagram for a rectangular lattice.

To find the direction of the energy in the lattice, the dispersion relation of the lattice needs to be calculated. To do so, we need to first find the differential equation for the lattice cell. Fig. 3 shows the unit cell for the rectangular lattice. By applying KVL and KCL to the unit cell, we have

$$LC \frac{d^2 V(l_1, l_2)}{dt^2} = V(l_1 + 1, l_2) + V(l_1 - 1, l_2) + V(l_1, l_2 + 1) + V(l_1, l_2 - 1) - 4V(l_1, l_2). \quad (8)$$

Now, if a plane-wave voltage of the form (4) is assumed for the node voltages in (8), it can be shown that the dispersion relation is

$$\omega = \frac{2}{\sqrt{LC}} [\sin^2(k_1/2) + \sin^2(k_2/2)]^{1/2}. \quad (9)$$

Relation (9) shows the nonlinear relationship between the wave vector  $\vec{a}$  and the frequency. This fundamentally comes from the discrete nature of the lattice. In electrical lattices usually one of the  $k_1$  or  $k_2$  is defined by the boundary conditions. Fig. 4 is the plot of  $k_1$  versus  $k_2$  for different frequencies. This graph is known as the *equi-frequency diagram*. The top right dot in the graph corresponds to the cutoff frequency of the lattice, which is achieved when  $k_1$  and  $k_2$  reach their maximum value

$$\omega_{\text{cut}} = \frac{2\sqrt{2}}{\sqrt{LC}}. \quad (10)$$

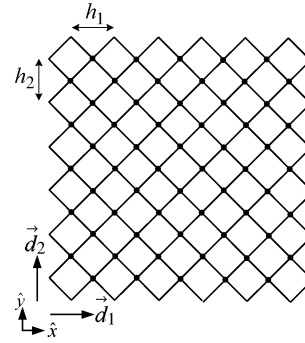


Fig. 5. Triangular LC lattice.

In a 2-D lattice, the cutoff frequency is a function of the direction of the wave vector. The cutoff frequency in (10) is the highest frequency that can propagate in the lattice, and at the cutoff frequency  $\angle \vec{a} = \pi/4$  if  $h_1 = h_2$ . In today's CMOS processes, if we use transmission lines as inductors and metal-to-metal capacitance as capacitors,  $L$  and  $C$  values can be as low as 20 pH and 5 fF. This will result in a cutoff frequency of 1.4 THz. Below these values, the inductance and capacitance will be dominated by the parasitics.

In a lossless lattice, the energy flow direction is the same as the direction of the group velocity. Using (9), group velocity can be shown to be

$$\vec{V}_g = \nabla_{\frac{k_1}{h_1}, \frac{k_2}{h_2}} \omega = h_1 \frac{\sin k_1}{\omega LC} \hat{x} + h_2 \frac{\sin k_2}{\omega LC} \hat{y}. \quad (11)$$

From (11), the direction of the energy is easily found to be

$$\text{Energy Direction} = \angle \vec{V}_g = \tan^{-1} \left( \frac{h_2 \sin k_2}{h_1 \sin k_1} \right). \quad (12)$$

If  $h_1 = h_2$ , by definition the group velocity direction is the direction of the perpendicular line to the equi-frequency curves in Fig. 4. For low frequencies,  $k_1$  and  $k_2$  are small, and the equi-frequency curves are close to a circle. Therefore, the energy direction is approximately equal to the wave vector  $\vec{a}$  direction (e.g., phase velocity direction). The energy direction is specified for two points in Fig. 4.

It can also be concluded from Fig. 4 that if  $k_1$  and  $k_2$  are positive—in other words, if  $\vec{a}$  has a positive phase between 0 and  $\pi/2$ —the group velocity  $\vec{V}_g$  also would have a phase between 0 and  $\pi/2$ . This is the reason that the rectangular lattice has a positive effective index over all of the frequencies. Any positive incident angle results in a positive transmission angle in this lattice.

### B. Triangular Lattice

Fig. 5 shows a right isosceles triangular lattice that is a  $45^\circ$  rotation of a square lattice. A square lattice is a rectangular lattice in which  $h_1 = h_2$ . In Fig. 5,  $\vec{d}_1$  and  $\vec{d}_2$  are the basis vectors and  $h_1$  and  $h_2$  are the node distances in the  $\hat{x}$ - and  $\hat{y}$ -directions, respectively. Due to the symmetry in this lattice,  $h_1 = h_2$ . For this triangular lattice, we can use exactly the same analysis as in Section II-A. The only difference is that, in (1c),  $l_1$  and  $l_2$  are not integers anymore. To be able to point to all of the nodes

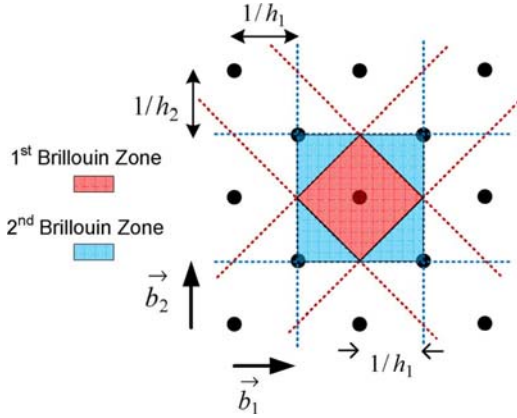


Fig. 6. Brillouin zones in reciprocal lattice for the triangular lattice.

with the specified basis vectors, we need to define  $l_1$  and  $l_2$  as follows:

$$\vec{r} = l_1 \vec{d}_1 + l_2 \vec{d}_2 \quad (13a)$$

$$l_1 = n/2 \quad l_2 = m/2; \quad n, m = \text{both odd or even.} \quad (13b)$$

Having the lattice set up, we can construct the reciprocal lattice for the triangular lattice. Fig. 6 shows this reciprocal lattice and the Brillouin zones in the lattice. In the first Brillouin zone, the maximum values for  $a_1$  and  $a_2$  are  $1/h_1$  and  $1/h_2$ , respectively. Using (5), we can find the maximum values for  $k_1$  and  $k_2$  in the first Brillouin zone

$$\text{Max}\{k_1\} = 2\pi \text{Max}\{a_1\} h_1 = 2\pi \quad (14a)$$

$$\text{Max}\{k_2\} = 2\pi \text{Max}\{a_2\} h_2 = 2\pi. \quad (14b)$$

Using the triangular lattice cell in Fig. 7 and (4) for a plane wave, the dispersion relation for a triangular LC lattice can be derived as

$$\omega = \frac{2}{\sqrt{LC}} \left[ \sin^2 \left( \frac{k_1 + k_2}{4} \right) + \sin^2 \left( \frac{k_1 - k_2}{4} \right) \right]^{1/2}. \quad (15)$$

The cutoff frequency is the same as (10), but when we rotated the lattice by  $45^\circ$ ,  $\angle \vec{a} = 0$ , or  $\pi/2$  instead of  $\pi/4$  in a square lattice at the cutoff frequency. Having (15), we can plot the equi-frequency diagram in Fig. 8. In this case, there are two solutions for  $k_1$  and  $k_2$  for each frequency. The curves start from  $\omega = 0.3\omega_{\text{cut}}$  at the upper right and lower left of the graph and end at the points corresponding to  $\omega = \omega_{\text{cut}}$  at the lower right and upper left of the graph.

Using (15) and (11), the energy direction in this triangular lattice can be found to be

$$\angle \vec{V}_g = \tan^{-1} \left( \frac{\sin \left( \frac{k_1 + k_2}{2} \right) - \sin \left( \frac{k_1 - k_2}{2} \right)}{\sin \left( \frac{k_1 + k_2}{2} \right) + \sin \left( \frac{k_1 - k_2}{2} \right)} \right). \quad (16)$$

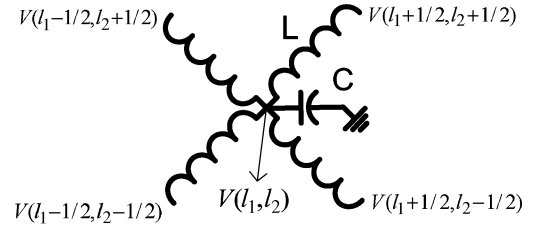


Fig. 7. Triangular lattice cell.

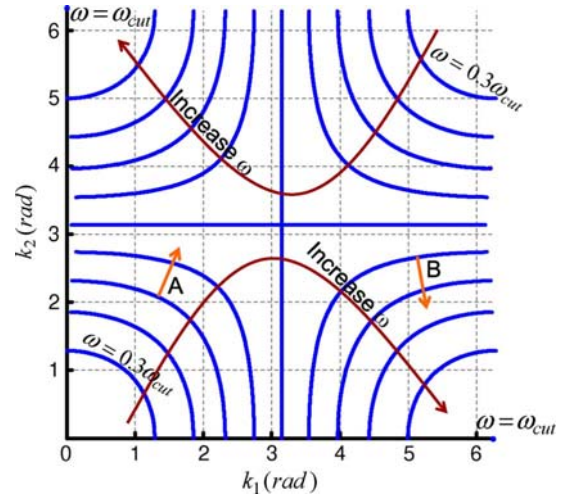


Fig. 8. Equi-frequency diagram for a triangular lattice.

In Fig. 8, the energy direction is specified in two points. For point A, the wave-vector phase  $\angle \vec{a}$  is between  $0$  and  $\pi/2$  as the energy direction. Therefore, at point A, the lattice has a positive effective index. This is true as long as  $k_1$  and  $k_2$  are less than  $\pi$ , but as soon as one of them exceeds  $\pi$ , then for positive  $\angle \vec{a}$ ,  $\angle \vec{V}_g$  will be negative. This implies a negative effective index for the lattice. Point B is the example of an operating point in which the lattice has a negative effective index.

### III. ELECTRICAL PRISM

#### A. Rectangular Lattice + Triangular Lattice

The electrical prism can be made by connecting a rectangular lattice and a triangular lattice together. Fig. 9 shows the prism in which the rectangular and triangular lattices have a  $45^\circ$  interface. Different interface angles other than  $45^\circ$  can also be visualized, but in implementation they are either too complicated or just too big for on-chip realization. In Fig. 9, the blue lattice (in the online version) is a rectangular lattice and the red lattice (in the online version) is a triangular lattice that is rotated by  $45^\circ$ .  $L_1$  and  $C_1$  are the inductor and capacitor for the rectangular lattice, and  $L_2$  and  $C_2$  are the inductor and capacitor for the triangular lattice. The plane wave is flowing from left to right in the rectangular lattice and has an incident angle  $\theta_i$  of  $45^\circ$  at the interface. The choice of this incident angle eliminates the use of wideband phase shifters at the boundary and leads to a simpler realization. In Fig. 9,  $k_1$  and  $k_2$  are the phase shift per section in the rectangular lattice in the  $\hat{x}$ - and  $\hat{y}$ -directions, respectively, while  $k_p$  is the phase shift per section along the interface and  $k_n$

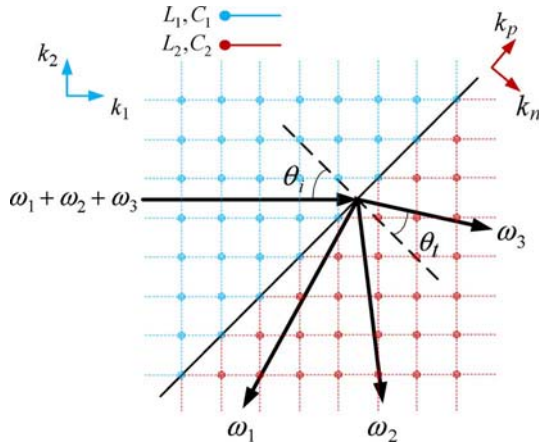


Fig. 9. Electrical prism using a rectangular and a triangular lattice.

is the phase shift per section perpendicular to the interface in the triangular lattice. In both lattices, we assume  $h_1 = h_2$ .

Since  $\theta_i = 45^\circ$ , it is clear from Fig. 9 that  $k_2 = 0$ . To find the transmission angle, we need to first find  $k_1$ . From (9),  $k_1$  can be found to be

$$k_1 = 2 \sin^{-1}(\omega \sqrt{L_1 C_1} / 2) \quad (17)$$

where  $k_1$  is the phase shift per section along the  $\hat{x}$ -direction in the rectangular lattice. Since the traveling signal is a plane wave,  $k_1$  is also the phase shift between the consecutive nodes at the lattice interface. In the triangular lattice,  $k_p$  is the phase shift per section along the interface, and therefore,  $k_1 = k_p$ . Now, using (15) and (17), we can find  $k_n$  to be

$$k_n = 2 \cos^{-1} \left( \frac{1 - L_2 C_2 \omega^2 / 4}{\cos(\sin^{-1}(\omega \sqrt{L_1 C_1} / 2))} \right). \quad (18)$$

Equations (17) and (18) describe  $k_p$  and  $k_n$  as a function of lattice components and the signal frequency. In (16),  $k_1$  and  $k_2$  can be substituted by  $k_n$  and  $k_p$ , respectively, to find the transmission angle  $\theta_t$ . Fig. 10 shows the plot of  $\theta_t$  versus signal frequency for different  $F = L_2 C_2 / L_1 C_1$ . In order to minimize the reflection from the interface, the characteristic impedance of both the lattices should be equal. It is not trivial to calculate the characteristic impedance of a 2-D lattice, especially for frequencies close to the cutoff frequency. The characteristic impedance is a function of the plane-wave propagation direction, and it is also a function of the signal frequency if it is close to the cutoff frequency. For a rectangular lattice, if the propagation direction is along the  $\hat{x}$  or  $\hat{y}$  axis, the characteristic impedance is  $\sqrt{L/C}$  for low-signal frequencies. The characteristic impedance of both lattices is kept constant at  $50 \Omega$ , and hence,  $Z_o = \sqrt{L_1/C_1} = \sqrt{L_2/C_2} = 50 \Omega$ . In Fig. 10,  $\omega_{cut2}$  is the cutoff frequency of the triangular lattice. As was mentioned in Section II, in today's CMOS processes, this cutoff frequency can be as high as 1.4 GHz. That is the main reason why this filter can operate at terahertz frequencies.

Fig. 10 shows that for a specific  $F$  factor, as the frequency increases,  $\theta_t$  and the derivative of the line gets more negative. This suggests that the separation of the frequencies increases at higher frequencies. More frequency separation can also be

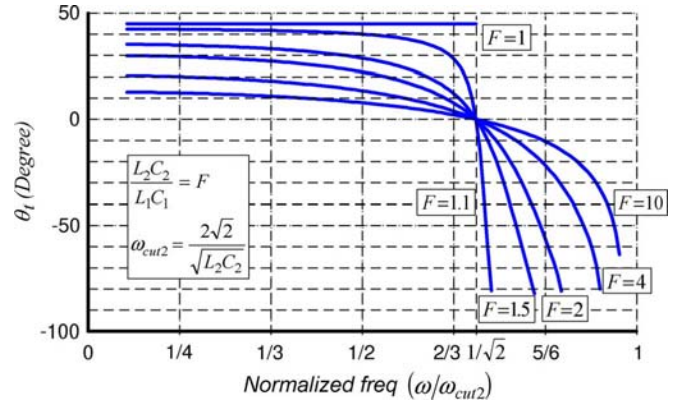


Fig. 10. Theoretical plot of frequency versus transmission angle for Fig. 9.

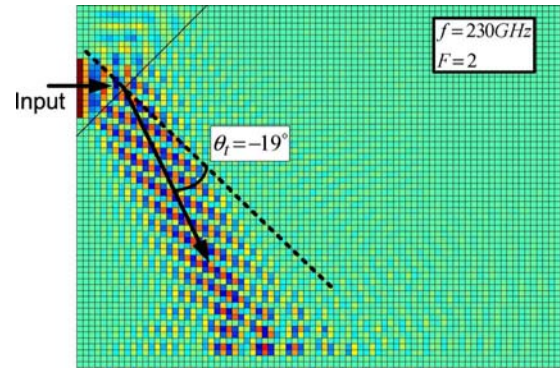


Fig. 11. MATLAB circuit simulation for a lossless lattice.

observed for the lower  $F$  factor as the line becomes steeper for those curves. If the output of the filter is fixed to a point on the triangular lattice, more frequency separation translates into a higher quality factor for the filter. The frequency point that all the curves intersect is the cutoff frequency of the triangular lattice when the signal is traveling in the  $\hat{x}$ - or  $\hat{y}$ -direction in Fig. 10. This can be seen in the trivial case of  $F = 1$  as the signal stops propagating at the same frequency. The negative effective index is also observed since the incident angle is  $45^\circ$  and the transmission angle is negative. For low frequencies, the transmission angle reaches a constant number, which is the exact angle that we can find from Snell's law

$$\frac{\sin \theta_i}{\sin \theta_t} = \frac{n_2}{n_1} = \frac{\sqrt{L_2 C_2}}{\sqrt{L_1 C_1}} = \sqrt{F}. \quad (19)$$

This validates the fact that, at low frequencies, refraction is the dominant effect in the energy direction, but as frequency grows, the wavelength becomes comparable to the lattice's dimension and dispersion plays the dominant role in the energy direction.

To validate this theory, a MATLAB code is used to solve for the differential equations in the lossless  $LC$  lattice and simulate the exact  $LC$  circuit. Ten equi-phase sources are applied to the left side of the rectangular lattice to create a plane wave and the two lattices combined have  $60 \times 80$  sections. A large lattice is used to better illustrate the direction of the energy. Fig. 11 shows the profile of the signal as it propagates through both lattices, with the red color (in the online version) the highest and blue color (in the online version) the lowest amplitude. The signal frequency

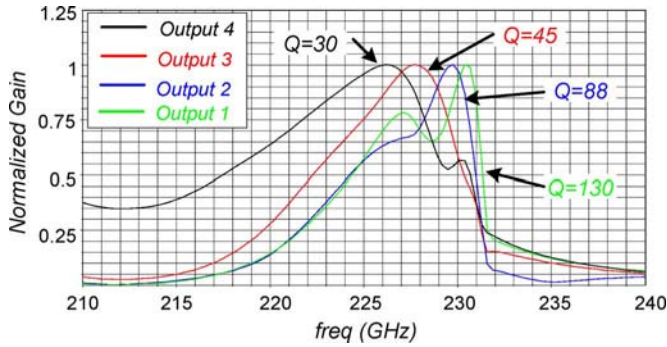


Fig. 12. Filter  $Q$  simulation using Cadence ( $F = 1.2$  and  $LC$  section  $Q = 10$ ).

is 230 GHz and the  $F$  factor is 2 in this figure. The characteristic impedance of both lattices is  $50 \Omega$  and the cutoff frequency of the triangular lattice is assumed to be 300 GHz. Therefore,  $L_2$  and  $C_2$  can be calculated to be 75 pH and 30 fF. The propagation direction in Fig. 11 is defined to be the direction that the maximum amplitude is traveling. The simulated  $\theta_t$  is  $-19^\circ$  and the theoretical  $\theta_t$  from Fig. 10 is  $-20^\circ$ . The direction of the energy was also simulated for some other frequencies, and they are either exactly the same or just  $1^\circ$  away from the theoretical value. The  $1^\circ$  difference can be explained by the transmission angle measurement error in the simulation. Fig. 11 also shows the channeling property of the lattice. It can be observed that because the frequency is close to the cutoff frequency, the signal is not propagating all over the lattice and channels to a specific direction. Intuitively, because the cutoff frequency is a function of energy direction, the signal dies out faster at directions other than the propagation direction in high frequencies. This has a significant effect on the quality factor of the filter. If the frequency was much lower than the cutoff frequency, as soon as the wave hits the interface, all of the nodes would act as point sources and a considerable amount of energy would spread out to most of the output nodes. The width of the signal ray is defined as the extent that the amplitude drops 3 dB from the maximum amplitude. In Fig. 11, because the lattice is lossless and the frequency is close to the cutoff, the width of the signal ray remains almost constant from the interface to the output. In Section IV-B, we will investigate the effect of loss on the width of the signal ray.

To find out the quality factor of the filter, the same lattice was constructed in Cadence. The  $LC$  section quality factor is chosen to be the typical on chip value of 10 at 230 GHz and the  $F$  factor is 1.2. The outputs of the filter are four fixed points at the boundary of the triangular lattice. Fig. 12 shows the normalized gain from input to output for different output nodes. The filter quality factor of 130 is achievable, which is much higher than the component quality factor of 10. This is not possible using classical filter design methods. For a given  $LC$  section quality factor ( $Q$ ), the quality factor of the filter will be a function of the size of the lattice—the larger the size, the greater the frequency separation, and hence, the better the filter quality factor. Of course, the larger the size, the higher the insertion loss would be. Fortunately, the size of the lattice is scaled down as the frequency of the operation goes up. This is because the inductor

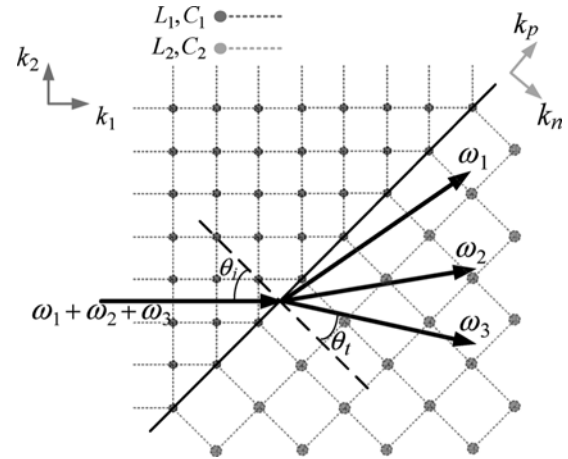


Fig. 13. Electrical prism using two rectangular lattices.

value decreases to support the higher frequency, and hence, reduces the size of the inductor and the overall lattice. This type of lattice is a strong candidate for high-frequency filtering as the  $Q$  of the components and the size of the lattice decreases.

#### B. Rectangular Lattice + Rectangular Lattice

The electrical prism can also be implemented by connecting two rectangular lattices together. Fig. 13 shows such a prism with the two rectangular lattices having a  $45^\circ$  interface. The theoretical analyses are exactly like the one in Section III-A. The major difference is that, in this kind of filter, there will be no negative effective index as two rectangular lattices are being used. Thus, at low frequencies, there will be a constant positive  $\theta_t$ , and as the frequency increases,  $\theta_t$  and the slope of the curve will be more positive. Therefore, the filtering and channeling properties still exist, but with a positive transmission angle. There will be two drawbacks for this filter compared with the one in Section III-A. First, the negative  $\theta_t$  is not present in the filter operation, and hence, the span of transmission angle over the frequency range is less than the one in Section III-A; this leads to a lower  $Q$  for this filter. Second, with respect to a terahertz on-chip implementation, the filter in Section III-A is simpler to implement because the inductors in both lattices are in the same direction and there is no  $45^\circ$  angle in the layout.

### IV. EFFECT OF COMPONENT LOSS IN THE ELECTRICAL PRISM

In order to study the effect of the component loss on the filter quality factor, we should examine its effect on two important features in the electrical prism—the direction of the energy and the channeling effect in the presence of loss.

#### A. Effect of Component Loss on the Direction of Energy

To find the effect of loss on the direction of the energy, we first need to find the dispersion relation of the lattice. Fig. 14 shows the lossy triangular lattice cell.  $L$  and  $C$  are the inductor and capacitor values for each section, and  $R_L$  and  $R_C$  are the resistors in parallel with the inductor and capacitor, respectively. By changing  $R_L$  and  $R_C$ , we can control the quality factor of the inductor and capacitor independently. Using the same analysis as in Section III, we can find the dispersion relation for the lossy

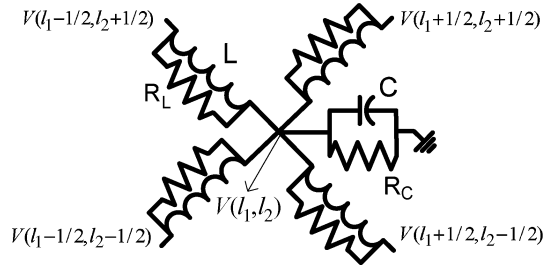


Fig. 14. Lossy triangular lattice cell.

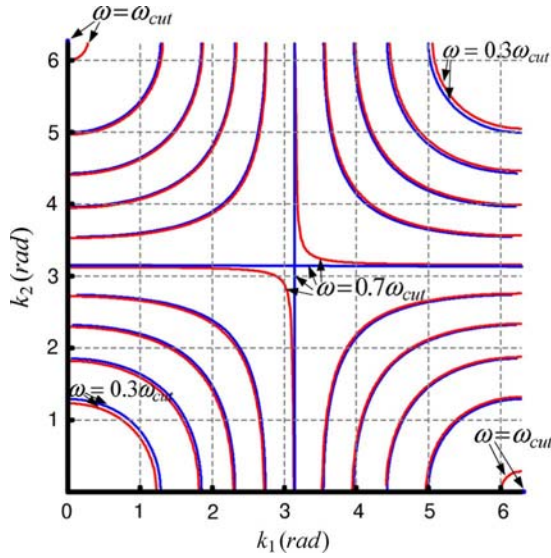


Fig. 15. Equi-frequency diagram of lossy (red in online version) versus lossless (blue in online version) triangular lattice.

triangular lattice. The only difference is that the voltage at each node is of the form

$$V = A \exp[-(\alpha_1 l_1 + \alpha_2 l_2)] \exp[i(k_1 l_1 + k_2 l_2 - \omega t)]. \quad (20)$$

where  $\alpha_1$  and  $\alpha_2$  are the attenuation constants in the  $\hat{x}$ - and  $\hat{y}$ -directions, respectively, because in the triangular lattice, we are using the same inductor everywhere in the lattice,  $\alpha = \alpha_1 = \alpha_2$ . Using (20), we can find the dispersion relation for a lossy triangular lattice in (21), shown at the bottom of this page. It can be easily verified in the lossless case where  $R_L$  and  $R_C$  go to infinity,  $\alpha$  vanishes and the relation in (21) will be the same as the one in (15). Having (21), we can plot the equi-frequency diagram and compare it with that of a lossless lattice. Fig. 15 shows

the equi-frequency diagram for a lossy lattice in red (in the on-line version) and the one for a lossless lattice in blue (in the on-line version). To plot the curves for a lossy lattice in Fig. 15, the same 300-GHz cutoff frequency is assumed.  $L$  and  $C$  are also 75 pH and 30 fF considering the characteristic impedance of 50  $\Omega$ . The quality factors of the inductors,  $Q_L$ , and the capacitors,  $Q_C$ , are chosen to be the typical on chip values of 10 and 100, respectively. This means that  $R_L$  and  $R_C$  are changing for each frequency to maintain these chosen values for  $Q_L$  and  $Q_C$ . Since  $Q_L$  is much smaller than  $Q_C$ , the  $LC$  section quality factor is approximately the same as  $Q_L = 10$ . Although we have chosen the cutoff frequency in (10) to be 300 GHz, the actual cutoff frequency of the lossy lattice is more than the lossless one. This can be viewed in Fig. 15 because the red curve (in the online version) for  $\omega = \omega_{cut}$  is not a single point anymore. The cutoff frequency in (10) is calculated assuming a lossless lattice. The new cutoff frequency for the lossy lattice can be calculated by substituting  $k_1 = 2\pi$  and  $k_2 = 0$  in (21).

As was discussed before, the direction of the energy is the direction of the line perpendicular to the curves in the equi-frequency diagram. For most of the curves in Fig. 15, the red curve (in the online version) and the blue curve (in the online version) are very similar and close to each other. As the loss is added to the lattice, the curves are slightly shifted to where the lower-frequency curves used to be in the lossless lattice. As a result, the direction of the energy will not change significantly for most of the frequencies. However, the points close to the center of Fig. 15 may see a significant change in the direction of the energy as the loss is added to the lattice. These points are close to the curve representing  $\omega = 0.7\omega_{cut} = 210$  GHz. This frequency is the cutoff frequency of the triangular lattice if  $\angle \vec{a} = \pi/4$ . Now, if we look at Figs. 10 and 12, we can see that all of the frequencies in which the filter has a high quality factor are larger than 210 GHz. Thus, in conclusion, the direction of the energy for the frequencies of interest would not significantly change as the loss is added to the lattice. Simulation results also verify this fact.

### B. Effect of Component Loss on the Channeling Effect

It is complicated to theoretically analyze the effect of component loss on the channeling effect. In order to get a sense of what happens to the width of the signal ray in the presence of loss, the filter was simulated with two different  $LC$  section quality factors. The quality factor of the capacitors kept high in order for the  $Q_L$  to be dominant. By comparing the signal profile at the boundary, we can see how wide the signal ray becomes as the component loss changes. In this simulation, signal

$$\omega^2 = \frac{4 - (e^{-\alpha} + e^{\alpha}) \left( \cos\left(\frac{k_1 + k_2}{2}\right) + \cos\left(\frac{k_1 - k_2}{2}\right) \right)}{CL + \frac{L^2}{R_L R_C} - \frac{4L^2}{R_L^2} - \frac{L^2 (e^{-\alpha} + e^{\alpha}) \left( \cos\left(\frac{k_1 + k_2}{2}\right) + \cos\left(\frac{k_1 - k_2}{2}\right) \right)}{R_L^2}} \quad (21)$$

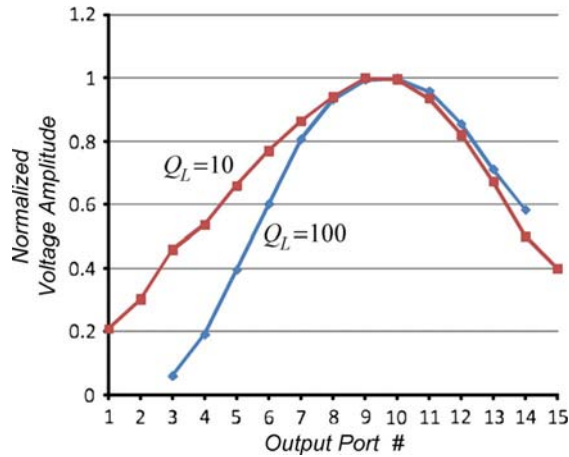


Fig. 16. Normalized voltage amplitude versus different output nodes for inductor quality factors of 10 and 100.

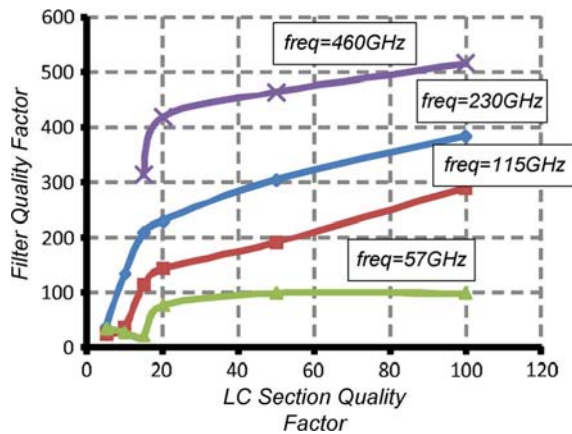


Fig. 17. Filter quality factor versus component quality factor.

frequency is 230 GHz and the  $F$  factor is 1.2. As before,  $L_2$  and  $C_2$  are 75 pH and 30 fF. The result of this simulation in Fig. 16 is the plot of normalized voltage amplitudes for different outputs at the boundary. The narrower this voltage profile is, the more channeled is the signal ray. It is clearly shown that for the higher component quality factor, the signal profile is narrower, and hence, more channeling is acquired. The narrower the signal ray, the higher the filter quality factor is achievable.

### C. Filter Quality Factor Versus Component Quality Factor

Fig. 17 shows the filter quality factor versus the  $LC$  section quality factor for different frequency bands. The ratio of  $LC$  product in two lattices,  $F$ , is kept constant at 1.2 for all four frequencies. As before,  $L_2$  and  $C_2$  are 75 pH and 30 fF for the 230 GHz. For the frequencies 460, 115, and 57 GHz,  $L_2$  and  $C_2$  are multiplied by half, two and four, respectively. To have a fair comparison, the physical size of the lattice is kept constant for all three frequencies. This means that the number of sections is reduced for lower frequencies to keep the same die size. We used  $95 \times 35$  sections for 460 GHz,  $60 \times 30$  sections for 230 GHz,  $38 \times 25$  sections for 115 GHz, and  $25 \times 20$  sections for 57 GHz. As a result, for a constant  $LC$  quality factor, the filter quality factor drops as the frequency drops. It is apparent from Fig. 17 that for a constant frequency, the filter quality factor decreases

as the component quality factor drops. This is expected because the channeling effect decreases as the component loss increases. This simulation shows that it is possible to get a quality factor of 420 at 460 GHz with a  $LC$  section quality factor of 20. The 460-GHz curve is not plotted for the  $LC$  section quality factor less than 15. The reason is that due to the large section number in this frequency (95 sections), for component quality factors less than 15, the loss is so high that the filter is not working properly. If we want to design a filter at 460 GHz with a component quality factor of less than 15, we should use a smaller lattice size. The following two important points can be derived from Fig. 17.

- For a constant die size, higher frequency filters will result in higher quality factors for the filters.
- We will achieve a higher quality factor boost ratio (the ratio of filter  $Q$  over component  $Q$ ), for the component quality factor of less than 20.

## V. ELECTRICAL PRISM IMPLEMENTATION

A 0.13- $\mu\text{m}$  CMOS process with seven metal layers was chosen to implement the electrical prism. As was discussed earlier, for the same filter quality factor, the size of the lattice decreases as the frequency increases. Thus, for the proof of concept, it is reasonable to choose the highest possible frequency to reduce the size as much as possible. A maximum frequency of 50 GHz was chosen due to the availability of the measurement tools and a relatively easier measurement setup compared with that of higher frequencies. To have high quality factor inductors,  $100 \mu\text{m} \times 100 \mu\text{m}$  spiral inductors were used for both rectangular and triangular lattices. The available die size of  $3.5 \text{ mm} \times 2.5 \text{ mm}$  along with the inductor size defines the number of sections to be  $18 \times 11$  for the electrical prism. The  $LC$  section quality factor is limited to the inductor quality factor in the 50-GHz range. At this frequency, the typical quality factor value for the spiral inductors in this process is around 20. Now, if we look at Fig. 17, for the 57-GHz curve we will get a filter quality factor of 70 if we use an inductor with a quality factor of 20, but for our implementation, both the frequency and lattice size are smaller than the 57-GHz curve in Fig. 17. Therefore, a filter quality factor of significantly less than 70 is expected, even with  $F = 1.2$ , which was used in Fig. 17. Based on Fig. 10, if a lower  $F$  factor is used, a higher filter quality factor is achievable, but an  $F$  factor less than 1.2 is not safe to use because the filter operation will be very sensitive to process variation. From Fig. 10, we know for  $F = 1.2$ , useful filtering is happening roughly between  $0.7\omega_{\text{cut}}$  and  $0.8\omega_{\text{cut}}$  because our maximum measurable frequency is 50 GHz,  $0.8\omega_{\text{cut}} = 50 \text{ GHz}$ . This will result in a triangular lattice cutoff frequency of around 60 GHz. For a cutoff frequency of 60 GHz and a characteristic impedance of  $50 \Omega$ , the inductor size for the triangular lattice will be 375 pH. In this process, the quality factor of a 375-pH inductor is around 10 at 50 GHz. In order to reduce the loss of the lattice, the characteristic impedance was reduced to  $30 \Omega$ . Now, the inductor size is 230 pH and the quality factor is around 20. In order to probe the signals at the input and output of the lattice, impedance-matching circuits

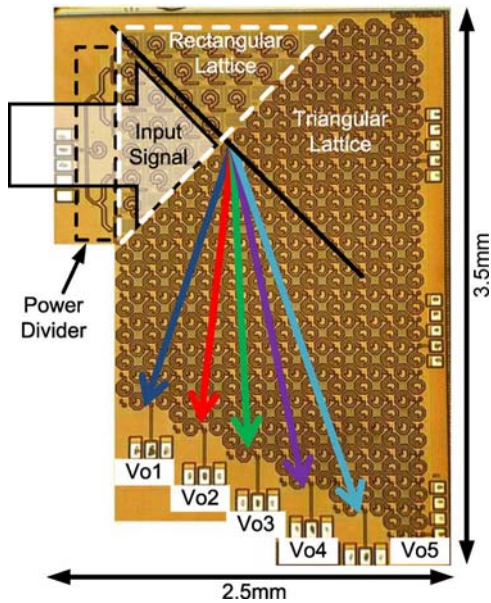


Fig. 18. Die picture.

were used to match  $30\text{--}50\ \Omega$ . The implemented electrical prism is shown in Fig. 18. A wideband one-to-eight power divider was designed to generate the eight equi-phase sources at the boundary of the rectangular lattice. Simulation shows that eight signal sources are good enough to generate a plane wave in the rectangular lattice. A 50-GHz signal source is used to apply the input signal to the lattice through the ground-signal-ground (GSG) pads. As previously mentioned, the inductors and capacitors for the triangular lattice are designed to be  $L_2 = 230\ \text{pH}$  and  $C_2 = 250\ \text{fF}$ . The inductors were implemented using spiral inductors with a quality factor of 20, and the capacitors were realized using MOS capacitors to get a quality factor of 80 for 50-GHz frequency. The outputs are probed at the bottom boundary of the triangular lattice through GSG pads. Five outputs is the maximum number we could have, given the size of the pads. In Fig. 18, the higher-frequency signals flow to  $V_{o1}$ , and the lower-frequency signals can be probed at  $V_{o5}$ . The attenuation constant for the higher-frequency signals flowing into  $V_{o1}$  is higher than the one at  $V_{o5}$ . Therefore, to equalize the voltage amplitudes at different outputs, the boundary was tilted. As is shown in Fig. 17, if the number of sections in the lattice and the component quality factor are low, having a low  $F$  factor will not improve the filter quality factor significantly. Thus, the  $F$  factor was optimized to get smooth filtering properties without sacrificing the filter quality factor. The best  $F$  is found to be 2.6. As a result, the inductors and capacitors for the rectangular lattice will be  $L_1 = 145\ \text{pH}$  and  $C_1 = 150\ \text{fF}$ . In the rectangular lattice, the vertical sections were removed to simplify the implementation, but that will not change anything because no signal is flowing into those sections.

Fig. 19 shows the simulation results for the five output nodes. This result includes the effect of all the parasitic capacitors and inductors in the layout. The graph shows the normalized gain from input to each output versus signal frequency. To better illustrate the frequency shift of the peaks, the normalized gain

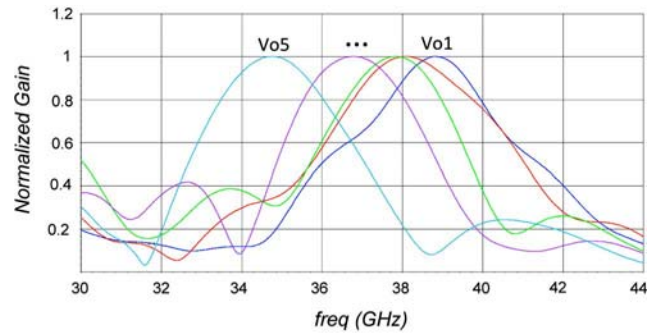


Fig. 19. Gain simulation results from input to each output.

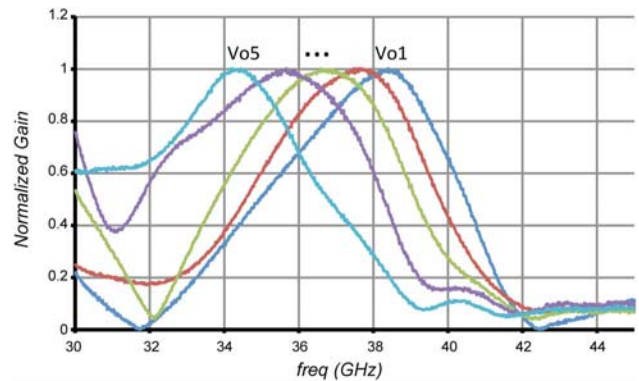


Fig. 20. Gain measurement results from input to each output.

was used. All of the peaks for the outputs are within 20% of the highest one in  $V_{o5}$  due to the boundary tilting. The signal peaks at about 34.5 and 38.5 GHz for  $V_{o5}$  and  $V_{o1}$ , respectively. Fig. 19 clearly shows the filtering behavior of the lattice and verifies the negative effective index for the lattice. The filter quality factors vary from 8 to 12 for different outputs. This is expected, based on the above discussion.  $V_{o1}$  has the highest and  $V_{o5}$  has the lowest filter quality factor. The insertion loss from each source at the boundary to each output is about 20 dB.

Fig. 20 presents the measurement results for the five output nodes. The results are very close to the simulation results. The peaks for different outputs are distributed over a 4-GHz span, as was done for the simulation in Fig. 19. Similarly, the peaks for all of the outputs are within 20% of the highest one. The filter quality factors is also very close to simulation and changes from 8 to 12 for different outputs.

## VI. CONCLUSION

Energy direction is a function of frequency in a low-pass 2-D lattice at frequencies close to the cutoff. This property can be exploited by implementing a high quality factor filter called an electrical prism. A negative effective index was shown to be achievable using this structure. Channeling of the signal and spatial filtering are the main reasons behind the filter having a higher quality factor than its component quality factors. Considering a fixed die size, the filter achieves higher quality factor values for terahertz frequencies. A prototype was designed and

measured to prove the feasibility of this approach. This structure is especially interesting because it is easy to fabricate using a conventional CMOS process.

#### ACKNOWLEDGMENT

The authors would like to thank G. N. Lilis, W. Lee, Y. Tousi, G. Li, and Prof. Rana, all with Cornell University, Ithaca, NY, for helpful discussions regarding various aspects of this work, and M. Azarmnia and M. Sharif for their support.

#### REFERENCES

- [1] P. H. Siegel, "Terahertz technology," *IEEE Trans. Microw. Theory Tech.*, vol. 50, no. 3, pp. 910–928, Mar. 2002.
- [2] T. W. Crowe, W. L. Bishop, D. W. Porterfield, J. L. Hesler, I. Weikle, and R. M. , "Opening the terahertz window with integrated diode circuits," *IEEE J. Solid-State Circuits*, vol. 40, no. 10, pp. 2104–2110, Oct. 2005.
- [3] K. B. Cooper, R. J. Dengler, G. Chattopadhyay, E. Schlecht, J. Gill, A. Skalare, I. Mehdi, and P. H. Siegel, "A high-resolution imaging radar at 580 GHz," *IEEE Microw. Wireless Compon. Lett.*, vol. 18, no. 1, pp. 64–66, Jan. 2008.
- [4] F. C. De Lucia, D. T. Petkie, and H. O. Everitt, "A double resonance approach to submillimeter/terahertz remote sensing at atmospheric pressure," *IEEE J. Quantum Electron.*, vol. 45, no. 2, pp. 163–170, Feb. 2009.
- [5] K. B. Cooper, R. J. Dengler, N. Lombart, T. Bryllert, G. Chattopadhyay, E. Schlecht, J. Gill, C. Lee, A. Skalare, I. Mehdi, and P. H. Siegel, "Penetrating 3-D imaging at 4- and 25-m range using a submillimeter-wave radar," *IEEE Trans. Microw. Theory Tech.*, vol. 56, no. 12, pp. 2771–2778, Dec. 2008.
- [6] *International Technology Roadmap for Semiconductors*, ITRS, 2007. [Online]. Available: [http://www.itrs.net/Links/2007ITRS/2007\\_Chapters/2007\\_Wireless.pdf](http://www.itrs.net/Links/2007ITRS/2007_Chapters/2007_Wireless.pdf)
- [7] D. Huang, T. R. LaRocca, M. C. F. Chang, L. Samoska, A. Fung, R. L. Campbell, and M. Andrews, "Terahertz CMOS frequency generator using linear superposition technique," *IEEE J. Solid-State Circuits*, vol. 43, no. 12, pp. 2730–2738, Dec. 2008.
- [8] E. Seok and K. K. O, "A 410 GHz CMOS push–push oscillator with an on-chip patch antenna," in *Proc. IEEE Int. Solid-State Circuits Conf. Tech. Dig.*, Feb. 2008, pp. 472–473.
- [9] E. Afshari, H. Bhat, X. Li, and A. Hajimiri, "Electrical funnel: A broadband signal combining method," in *Proc. IEEE Int. Solid-State Circuits Conf. Tech. Dig.*, Feb. 6–9, 2006, pp. 751–760.
- [10] H. S. Bhat and E. Afshari, "Nonlinear constructive interference in electrical lattices," *Phys. Rev. E, Stat. Phys. Plasmas Fluids Relat. Interdiscip. Top.*, vol. 77, no. 6, 2008, Art. ID 066602.
- [11] E. Afshari, H. S. Bhat, and A. Hajimiri, "Ultrafast analog fourier transform using 2-D LC lattice," *IEEE Trans. Circuits Syst. I, Reg. Papers*, vol. 55, no. 8, pp. 2332–2343, Sep. 2008.
- [12] G. V. Eleftheriades, A. K. Iyer, and P. C. Kremer, "Planar negative refractive index media using periodically LC loaded transmission lines," *IEEE Trans. Microw. Theory Tech.*, vol. 50, no. 12, pp. 2702–2712, Dec. 2002.
- [13] G. V. Eleftheriades and O. F. Siddiqui, "Negative refraction and focusing in hyperbolic transmission-line periodic grids," *IEEE Trans. Microw. Theory Tech.*, vol. 53, no. 1, pp. 396–403, Jan. 2005.
- [14] D. Sievenpiper, J. Schaffner, J. J. Lee, and S. Livingston, "A steerable leaky-wave antenna using a tunable impedance ground plane," *IEEE Antennas Wireless Propag. Lett.*, vol. 1, no. 1, pp. 179–182, 2002.
- [15] D. Smith and D. R. Schurig, "Electromagnetic wave propagation in media with indefinite permittivity and permeability tensors," *Phys. Rev. Lett.*, vol. 90, pt. 7, 2003, Art. ID 077405.
- [16] P. S. D. Smith and D. R. Kolinko, "Negative refraction in indefinite media," *J. Opt. Soc. Amer. B, Opt. Phys.*, vol. 21, pt. 5, pp. 1032–1043, 2004.
- [17] C. A. Desoer and S. K. Ernest, *Basic Circuit Theory*. New York: McGraw-Hill, 1969.
- [18] I. Aoki, S. D. Kee, D. B. Rutledge, and A. Hajimiri, "Fully integrated CMOS power amplifier design using the distributed active-transformer architecture," *IEEE J. Solid-State Circuits*, vol. 37, no. 3, pp. 371–383, Mar. 2002.
- [19] H. Kosaka, T. Kawashima, A. Tomita, M. Notomi, T. Tamamura, T. Sato, and S. Kawakami, "Superprism phenomena in photonic crystals: Toward microscale lightwave circuits," *J. Lightw. Technol.*, vol. 17, no. 11, pp. 2032–2038, Nov. 1999.
- [20] T. Matsumoto, T. Asatsuma, and T. Baba, "Experimental demonstration of a wavelength demultiplexer based on negative-refractive photonic-crystal components," *Appl. Phys. Lett.*, vol. 91, no. 9, 2007, Art. ID 091117.
- [21] M. Notomi, "Theory of light propagation in strongly modulated photonic crystals: Refractionlike behavior in the vicinity of the photonic band gap," *Phys. Rev. B, Condens. Matter*, vol. 62, pt. 16, pp. 10 696–10 705, 2000.
- [22] O. Momeni and E. Afshari, "Electrical prism: A high quality factor filter for mm wave and terahertz frequencies," in *IEEE Asia-Pacific Microw. Conf.*, Dec. 16–20, 2008, pp. 1–4.
- [23] K. Kittel, *Introduction to Solid State Physics*. New York: Wiley, 2004.
- [24] L. Brillouin, *Wave Propagation in Periodic Structures*. New York: Dover, 1946.



**Omeed Momeni** (S'03) received the B.Sc. degree in electrical engineering from the Isfahan University of Technology, Isfahan, Iran, in 2002, the M.S. degree in electrical engineering from the University of Southern California, Los Angeles, in 2006, and is currently working toward the Ph.D. degree at Cornell University, Ithaca, NY.

From May 2004 to December 2006, he was with the National Aeronautics and Space Administration (NASA), Jet Propulsion Laboratory (JPL), to design *L*-band transceivers for synthetic aperture radar (SAR) radars and high power amplifiers for Mass Spectrometer applications. His research interests include high-speed analog and RF integrated circuits.

Mr. Momeni was a recipient of the 2003 NASA–JPL Summer Fellowship and the 2007 Cornell University Jacob's Fellowship.



**Ehsan Afshari** (S'98–M'07) was born in Tehran, Iran, in 1979. He received the B.Sc. degree in electronics engineering from the Sharif University of Technology, Tehran, Iran, in 2001, and the M.S. and Ph.D. degrees in electrical engineering from the California Institute of Technology, Pasadena, in 2003 and 2006, respectively.

In August 2006, he joined the faculty of the Department of Electrical and Computer Engineering, Cornell University, Ithaca, NY.

Prof. Afshari was the recipient of the 2008 Defense Advanced Project Agency (DARPA) Young Faculty Award and Iran's 2001 Best Engineering Student Award by the President of Iran. He was also the recipient of the Best Paper Award presented at the 2003 Custom Integrated Circuits Conference (CICC), First Place at the 2005 Stanford–Berkeley–Caltech Inventor's Challenge, the 1999 Best Undergraduate Paper Award presented at the Iranian Conference on Electrical Engineering, the 1997 Silver Medal of the Physics Olympiad, and the 2004 Award of Excellence in Engineering Education presented by the Association of Professors and Scholars of Iranian Heritage (APSIH).